

Development of a multi-compartment population balance model for high-shear wet granulation with Discrete Element Method

Kok Foong Lee¹, Maksym Dosta³, Andrew D. McGuire¹, Sebastian Mosbach¹, Wolfgang Wagner⁴, Stefan Heinrich³, Markus Kraft^{1,2}

released: 4 July 2016

¹ Department of Chemical Engineering and Biotechnology
University of Cambridge
New Museums Site
Pembroke Street
Cambridge, CB2 3RA,
United Kingdom.

² School of Chemical and Biomedical Engineering
Nanyang Technological University
62 Nanyang Drive,
Singapore, 637459.

³ Institute of Solids Process Engineering and Particle Technology,
Hamburg University of Technology,
Denickestrasse 15,
21073 Hamburg, Germany.

⁴ Weierstrass Institute for Applied Analysis and Stochastics,
Mohrenstraße 39,
10117 Berlin,
Germany.

Preprint No. 170



Keywords: granulation, stochastic weighted algorithm, compartmental model, discrete element method, majorant kernel

Edited by

Computational Modelling Group
Department of Chemical Engineering and Biotechnology
University of Cambridge
New Museums Site
Pembroke Street
Cambridge CB2 3RA
United Kingdom

Fax: + 44 (0)1223 334796

E-Mail: c4e@cam.ac.uk

World Wide Web: <http://como.cheng.cam.ac.uk/>

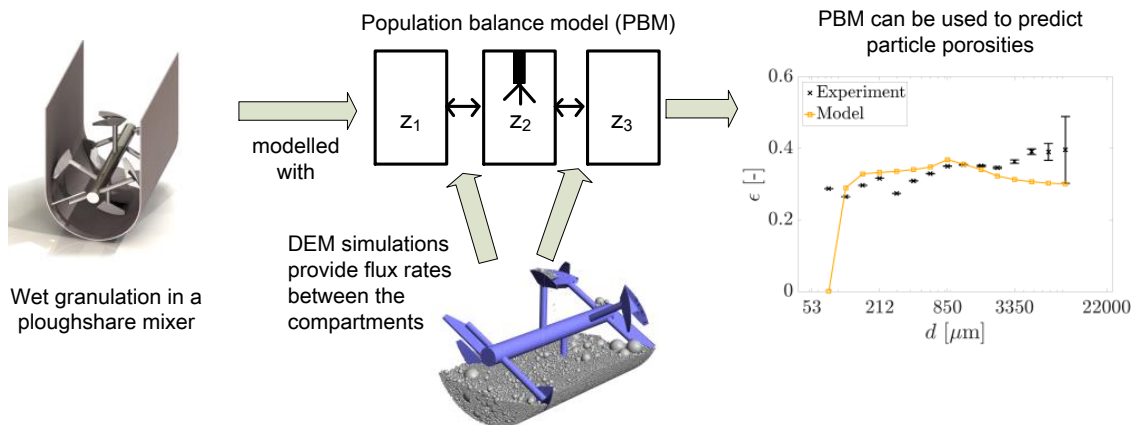


Highlights

- A granulation process is modelled using a population balance model (PBM) and DEM.
- Particles in the population balance model are five-dimensional.
- The population balance model has 3 compartments to consider spatial inhomogeneity.
- The PBM is used to model particle size and porosity distributions.
- The performance of the PBM is improved by utilising information from DEM.

Abstract

This paper presents a multi-compartment population balance model for wet granulation coupled with DEM (Discrete Element Method) simulations. Methodologies are developed to extract relevant data from the DEM simulations to inform the population balance model. First, compartmental residence times are calculated for the population balance model from DEM. Then, a suitable collision kernel is chosen for the population balance model based on particle-particle collision frequencies extracted from DEM. It is found that the population balance model is able to predict the trends exhibited by the experimental size and porosity distributions by utilising the information provided by the DEM simulations.



Contents

1	Introduction	3
2	Multi-compartment population balance model	4
2.1	Type-space	4
2.2	Particle processes	5
3	DEM	7
3.1	Compartmental residence times	8
3.2	Collision rate function	11
4	Numerical method for the population balance model	14
4.1	Liquid addition	15
4.2	Breakage	15
4.3	Particle transport	16
4.4	Collision	16
4.4.1	Size independent	18
4.4.2	Equipartition of kinetic energy (EKE)	18
4.5	Simulation algorithm	19
5	Application	20
6	Conclusions	24
	References	24
A	Derivation of three compartment mixing model	30

1 Introduction

Wet granulation is a manufacturing process to produce granules with desired properties from small particles and binders, using equipments such as high-shear mixers, rotating drums and fluidised beds. Models for granulation can be broadly separated into particle level models and models which simulate the process at the unit operation level [27, 42]. Models at the particle level are developed to predict inter-particle forces using fundamental physics and a review of such models can be found in [31]. At the other end of the scale, models at the unit operation level are used to predict the overall behaviour of granulation processes and this paper focuses on this aspect. Modelling approaches for wet granulation processes at the unit operation level can be loosely separated into two categories: population balance modelling and Discrete Element Method (DEM).

The population balance approach tracks the change in the particle population with time through birth and death processes, for applications in granulation, these processes are usually the coalescence and breakage of particles [7]. Traditionally, population balance models are one-dimensional with particle size as the focus. However, one-dimensional models are insufficient to describe granulation processes accurately [30]. Hence, over the last decade, population balance models published in the literature have been at least two-dimensional with liquid and solid concentrations as the properties included [1, 39, 44] and some models also include particle pore volume [14, 18, 48]. The main advantage of the population balance approach is that it is capable at considering detailed physical models for processes such as coalescence [14, 18, 38, 39], nucleation [44, 48] and breakage [49]. Population balance modelling is also suitable for long time scale studies because of its low computational effort, but it requires certain knowledge of the system in order to include the appropriate processes.

In DEM simulations, the motion of each particle is computed simultaneously using Newtonian equations of motion [13]. It is pointed out in [42] that models at the unit operation level often neglect the flow heterogeneity of powder mixing processes and the DEM approach seems to be the ideal solution to bridge this gap. However, DEM is computationally expensive and it does not consider aggregation of granules and other processes such as solidification of granules [1].

Nonetheless, it is possible to include particle flow in population balance models. This is done by dividing the simulation domain into multiple compartments with each of them having its own population balance equation. Thus, each compartment is considered to be perfectly mixed but the process rates can differ between the compartments. A main drawback of this approach is that the flux rates between the compartments are unknown but these can be determined by coupling DEM to population balance models. Population balance models that involve DEM simulations generally fall into three categories: Models that use post-processed flux rates from preliminary DEM simulations [5, 15, 23, 37, 53], models that utilise DEM to develop appropriate aggregation kernels [24, 55], and models that are directly coupled with DEM [1–3]. The work carried out in this paper falls into the first two categories.

The main purpose of this paper is to improve an existing multi-compartment population balance model for a batch ploughshare mixer [35, 36] with post-processed information

from DEM simulations. Previously, the residence times of the compartments were unknown and they were tuned to fit an experimentally measured size distribution. Besides that, the existing model uses a size independent collision kernel and it is found that it is inappropriate for granulation systems [24]. In this paper, DEM simulations are performed to determine the appropriate residence times for the compartments and also to implement a size dependent collision kernel.

This paper is organised as follows: A brief description of the population balance model is given in Section 2. Then, Section 3 outlines the DEM simulations carried out in this work. Section 4 describes the stochastic particle method used to solve the population balance model, in particular the adaptation of the majorant technique [20, 25, 40, 47] to accelerate the simulation of collision events. Finally, the ability of the population balance model to predict a set of experimental results is assessed in Section 5.

2 Multi-compartment population balance model

The experimental system considered in this work is the wet granulation of lactose powder with deionised water carried out in a ploughshare mixer depicted in Figure 1 and its full description can be found in [34]. It is modelled as a series of well-mixed continuous-stirred tank reactors (CSTRs) to account for spatial inhomogeneity and each reactor in the network is given a characteristic residence time, τ . The configuration of the compartmental model is shown in Figure 2. As previous studies showed that radial dispersion is significantly quicker compared to axial dispersion [12, 32, 33], the mixer is compartmentalised in the axial direction in the model. The multi-compartment population balance model was developed in [35, 36], but the residence times of the compartments were not known and the values were tuned to fit an experimentally measured particle size distribution. In this work, the residence times of the compartments are determined using DEM and the methodology is presented in Section 3.1.

In the model, particles take positions in a domain of compartments, $\mathbb{Z} = \{z_1, z_2, z_3\}$. Throughout this work, the residence times of z_1 , z_2 , and z_3 are denoted as τ_1 , τ_2 , and τ_3 respectively. In order to capture the spreading of binder liquid which is often regarded as a crucial stage in granulation processes [22, 31, 50], the middle compartment z_2 is defined as the spray zone where liquid addition occurs. With the exception of liquid addition, each compartment simulates the same particle processes described in Section 2.2, but at different rates to capture the spatial inhomogeneity of the process.

2.1 Type-space

The type-space is the mathematical description of a particle. In this model, the type-space $\mathbb{X} = \{s_o, s_r, l_e, l_i, p\}$ has five independent non-negative variables which describe a granule. They are original solid volume s_o , reacted solid volume s_r , external liquid volume l_e , internal liquid volume l_i , and pore volume p . Particle properties such as volume v , mass m , diameter d , and porosity $\varepsilon = \frac{p}{v}$ can be calculated from these internal variables. To calculate the diameter, granules are assumed to be spherical.

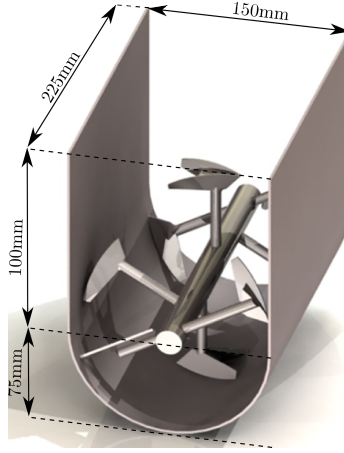


Figure 1: CAD drawing of the mixer. The radial direction refers to direction in which the blades rotate and the axial direction refers to the direction along the shaft.

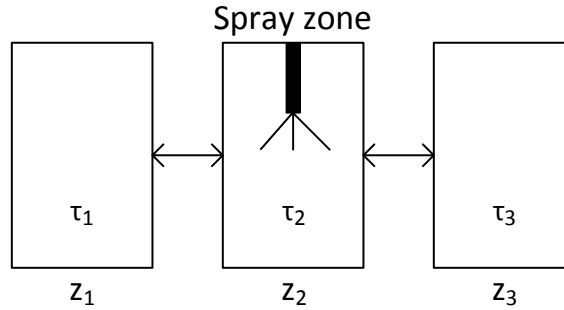


Figure 2: Configuration of the compartmental model. The mixer (Figure 1) is compartmentalised in the axial direction. Each compartment has the same size.

2.2 Particle processes

In this model, particles may be created and evolved through several different processes. Most of the processes are described briefly here. For the full description of the model and the reasoning behind the submodels, readers can refer to [6–11].

Liquid addition: Liquid droplets are introduced into the particle ensemble in the form of

$$x_{\text{droplet}} = (0, 0, l_e, 0, 0),$$

at the rate

$$r_{z, \text{droplet}} = \begin{cases} \frac{\dot{V}_1}{V_{\text{droplet}}} & , \text{ if } z = z_2, \\ 0 & , \text{ otherwise,} \end{cases} \quad (1)$$

where \dot{V}_1 is the volumetric flow rate of the binder (experimental condition) and V_{droplet} is the droplet volume.

Breakage: The current model considers a binary breakage process [9]:

$$(x_i) \rightarrow (x_j), (x_i - x_j), \quad (2)$$

and each particle x_i breaks at the frequency

$$r_{z, \text{break}}(x_i) = \begin{cases} k_{z, \text{break}} U_{\text{imp}}^2 (p + l_e) & , \text{ if } v(x_i) \geq v_{\text{parent, min}}, \\ 0 & , \text{ otherwise.} \end{cases} \quad (3)$$

with input parameters $k_{z, \text{break}}$ (breakage rate constant which may differ in different compartments) and U_{imp} (impact velocity between the particles and impeller blades). $v_{\text{parent, min}}$ is the smallest parent particle that can undergo breakage.

Chemical reaction: The liquid components (l_e and l_i) are transformed into reacted solid, s_r , at the rate

$$r_{z, \text{reac}}(x) = \begin{cases} k_{z, \text{reac}} a_e(x) \frac{l_e}{l_e + s_r}, & \text{for } l_e \rightarrow s_r \\ k_{z, \text{reac}} a_i(x) \frac{l_i}{l_i + s_r}, & \text{for } l_i \rightarrow s_r, \end{cases} \quad (4)$$

where a_e and a_i are the external and internal surface areas respectively. $k_{z, \text{reac}}$ is the reaction rate constant which may differ in different compartments. This work studies the granulation of lactose powder with deionised water. Without the presence of lactase, the only reaction is the hydration of lactose by water [56].

Penetration: This process refers to the diffusion of external liquid into the pores, i.e. transformation of l_e into l_i , and occurs at the rate

$$r_{z, \text{pen}}(x) = k_{z, \text{pen}} \eta^{-0.5} l_e (p - l_i), \quad (5)$$

where $k_{z, \text{pen}}$ is the penetration rate constant which may differ in different compartments and η is the viscosity of the binder.

Particle transport: Each particle leaves its current compartment z at the rate

$$r_{z, \text{transport}} = \frac{1}{\tau_z}, \quad (6)$$

where τ_z denotes the residence time of compartment z .

Collision: The rate of collision between the particles x_i and x_j is defined by the kernel:

$$K_z(x_i, x_j) = \omega_{\text{impeller}} U_{\text{col}} k_{z, \text{col}} C(d_i, d_j), \quad (7)$$

where ω_{impeller} is the impeller speed, U_{col} is the particle-particle collision velocity, $k_{z, \text{col}}$ is the collision rate constant which may differ in different compartments, and $C(d_i, d_j)$ is the collision rate function which defines the collision frequency between particles with diameters d_i and d_j . In the original model [7–9], the collision kernel is independent of size and the collision rate function is first introduced in this work. In Section 3.1, a suitable size dependent collision rate function is determined with collision rates extracted from a DEM simulation.

Each collision leads to the compaction of the colliding particles and the change in porosity is described by

$$\Delta \epsilon(x) = \begin{cases} k_{z, \text{comp}} (\epsilon(x) - \epsilon_{\text{min}}) & , \text{ if } \epsilon(x) \geq \epsilon_{\text{min}}, \\ 0 & , \text{ otherwise,} \end{cases} \quad (8)$$

where $k_{z, \text{comp}}$ is the compaction rate constant which may differ in different compartments and ε_{min} is the minimum porosity. However, the success of coalescence is controlled by the collision efficiency \tilde{K} calculated based on the Stokes criterion [9, 21] which compares the kinetic energy of collision to the dissipation energy provided by the binder:

$$\tilde{K}(x_i, x_j) = \begin{cases} 1, & \text{(successful coalescence),} \\ 0, & \text{(unsuccessful coalescence).} \end{cases} \quad (9)$$

Depending on the value of $\tilde{K}(x_i, x_j)$, a collision between the particles x_i and x_j has the following outcomes

$$\begin{aligned} (x_i), (x_j) &\rightarrow T_{\text{comp}}(x_i + x_j), & \text{if } \tilde{K}(x_i, x_j) = 1, \\ (x_i), (x_j) &\rightarrow T_{\text{comp}}(x_i), T_{\text{comp}}(x_j), & \text{if } \tilde{K}(x_i, x_j) = 0, \end{aligned} \quad (10)$$

where T_{comp} represents the compaction process (8).

3 DEM

The DEM implementation in this paper uses the Hertz-Mindlin model for the calculations of both the particle-particle and particle-wall contact. For more details regarding the implementation, readers can refer to [19]. The geometry used in the DEM simulations is constructed to match the laboratory mixer and the CAD drawing is shown in Figure 1.

Dry spherical particles are used in the simulations and the effects of the binder liquid are ignored. DEM simulations are carried out in this work to provide two crucial information needed by the population balance model. The first piece of information is the residence times of the compartments and the second piece of information is the collision rates between particles as a function of size. The computational cost of a DEM simulation varies according to the simulation time required, number of particles and the range of particle size. In order to obtain reliable estimates of the residence times, it is necessary to perform the simulation for a long period of time. On the other hand, it is required to include a wide range of particle sizes to estimate the collision rate function but long simulation time is unnecessary. Therefore, two separate simulations with different specifications are performed to balance between what is achievable within reasonable computational costs and the quality of data obtainable.

The first DEM simulation is performed to estimate the residence times of the compartments. Uniformly sized large particles (2.6 mm) are used so that it is possible to simulate the system long enough. The number of particles is adjusted to match the bed volume in the experiments and this results in approximately 80,000 particles.

The second DEM simulation is carried out to estimate the collision rate function. Since it is unnecessary to simulate the system for that long, it is possible to increase the number of particles in the expense of CPU time for this simulation. The particles for this simulation are generated according to a measured size distribution obtained from the same experimental conditions described later in Section 5. To limit the number of particles, it is required to apply a lower cut off size of 1 mm and this resulted in approximately 200,000

particles. The experimental particle size distribution is shown later in Section 5 (Figure 9) where it is used to evaluate the performance of the population balance model to reproduce experimental results.

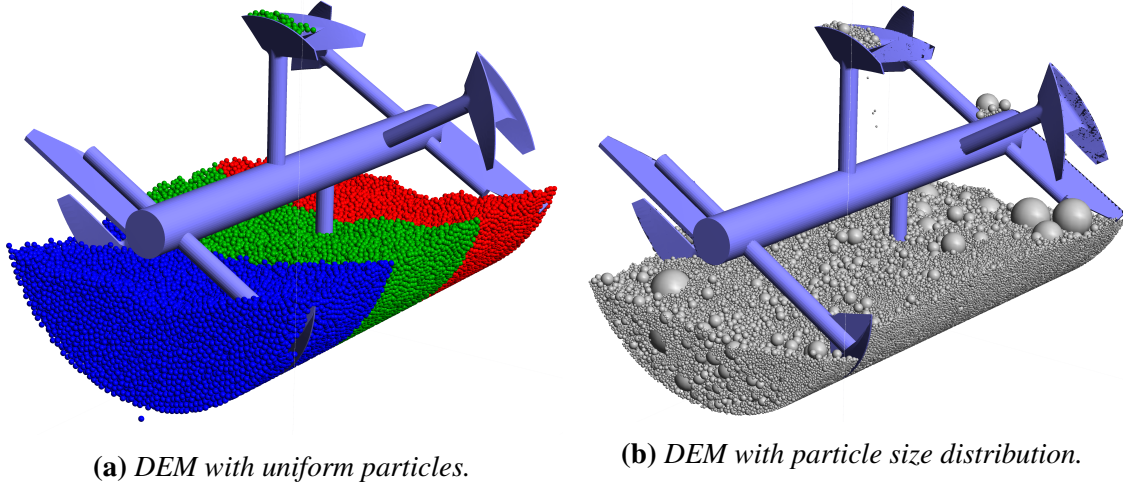


Figure 3: *Initial states of the DEM simulations. Particles are tagged with colours [red, green, blue] for the uniform case to determine the residence times in Section 3.1.*

Both case studies are simulated at the same impeller speed (2 rev/s) as the experimental system we are modelling (described later in Section 5) and the material properties used for the simulations are summarised in Table 1. Among the properties, the density, coefficient of restitution and Young’s Modulus are experimentally measured, and the rest are extracted from the literature. Dried lactose granules are used for the measurements and the effects of the binder are ignored. The coefficient of restitution of dried lactose granules is measured using an optical technique described in [17] and an average value of 0.2 is obtained from the measurements. The Young’s Modulus is calculated from single granule compression tests described in [52]. An average value of 1.7×10^7 Pa is used for the simulation with uniform particles and the values used in the simulation with the experimental particle size distribution are shown in Figure 4 where the Young’s Modulus is set according to the particle size.

3.1 Compartmental residence times

This section describes the methodology to estimate the residence times of the compartments using the DEM simulation with uniform particles (Figure 3a). The easiest way to calculate the residence time for a compartment is to evaluate the average duration a particle spends in the compartment before it exits the compartment. However, this approach is not suitable to derive representative residence times for the compartments because the frequency distribution of residence times is very wide as shown in Figure 5 for the compartment z_1 . To obtain the frequencies for the respective residence times, each time a particle passes through the boundary between z_1 and z_2 , the time spent by the particle

Table 1: *Material properties used in DEM. Values shown are for both simulations with uniform particle and PSD unless otherwise stated.*

Property	Value
Density of lactose	1545 kg m ⁻³
Coefficient of restitution	0.2
Coefficient of friction (particle-particle)	0.2
Coefficient of friction (particle-wall)	0.35
Poisson ratio [4]	0.3
Young's Modulus of lactose (uniform size)	1.7 × 10 ⁷ Pa
Young's Modulus of lactose (PSD)	Refer Figure 4
Young's Modulus of steel [4]	2.15 × 10 ¹¹ Pa

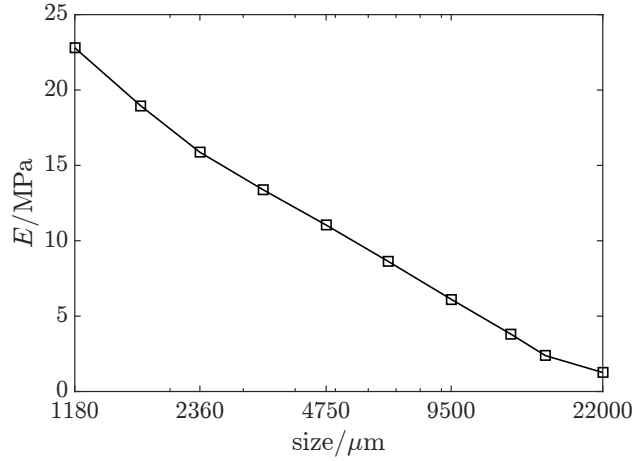


Figure 4: *Young's Modulus, E , used in the DEM simulation for the estimation of the collision rate function.*

in z_1 before returning to z_2 is recorded. The enormous frequencies recorded for short residence times are contributed by the particles oscillating at the border between z_1 and z_2 . From the plot, it can also be observed that there are particles which stayed in the same compartment for almost the entire simulation (system is simulated for 200 seconds). Therefore, it is not possible to calculate a reliable average residence time by tracking the actual residence times of the particles.

Instead, the compartmental residence times are estimated by considering the evolution of particle concentrations in the compartments and assuming each compartment is well-mixed. This is done by tagging the particles in each compartment with colours (z_1 : red, z_2 : green, z_3 : blue) as shown in Figure 3a at the beginning of the simulation. Then, the volume fraction of the colour c in compartment z at time t is calculated by

$$\hat{V}_{z,c}(t)_{\text{DEM}} = \frac{V_{\text{particle}}(t, z, c)}{\sum_c V_{\text{particle}}(t, z, c)}, \quad (11)$$

where $V_{\text{particle}}(t, z, c)$ is the total volume of particles of the colour c in compartment z at

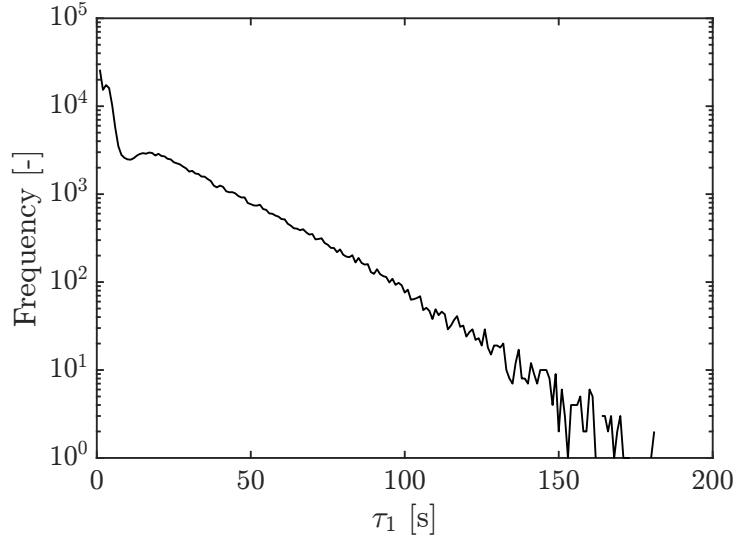


Figure 5: Residence time distribution for the compartment z_1 .

time t and $\sum_c V_{\text{particle}}(t, z, c)$ is the total volume of all the particles which is located in compartment z at time t .

The evolutions of the volume fractions in each compartment are fitted to a model which assumes an idealised reactor network. In the model, each compartment is assumed to be perfectly mixed with a tertiary particle colour system initially loaded as [red, green, blue]. It assumes that the separation between compartment boundaries is sufficiently large and the time step between analysis frames is sufficiently small such that particles cannot ‘skip’ over compartments (e.g. from z_1 directly to z_3). The model assumes constant mass, constant particle density and constant particle size in each compartment hold-up throughout the mixing process. The model was solved for the evolution of particle volume fraction \hat{v} for each colour c in each compartment z to yield four unique model equations:

$$\hat{v}_{1,\text{red}}(t)_{\text{model}} = \left[\frac{1}{2} \exp\left(-\frac{t}{\tau_1}\right) + \frac{1}{6} \exp\left(-\frac{3t}{\tau_1}\right) - \frac{2}{3} \right], \quad (12)$$

$$\hat{v}_{2,\text{red}}(t)_{\text{model}} = \left[-\frac{1}{3} \exp\left(-\frac{3t}{\tau_1}\right) + \frac{1}{3} \right], \quad (13)$$

$$\hat{v}_{3,\text{red}}(t)_{\text{model}} = \left[-\frac{1}{2} \exp\left(-\frac{t}{\tau_1}\right) + \frac{1}{6} \exp\left(-\frac{3t}{\tau_1}\right) + \frac{1}{3} \right], \quad (14)$$

$$\hat{v}_{2,\text{green}}(t)_{\text{model}} = \left[\frac{2}{3} \exp\left(-\frac{3t}{\tau_1}\right) - \frac{2}{3} \right], \quad (15)$$

similar to the residence times, the subscripts 1, 2, and 3 correspond to the compartments z_1 , z_2 , and z_3 .

Due to the symmetrical nature of both the mixture operation and loading it is known that

in an ideal system:

$$\hat{v}_{1,\text{blue}}(t) = \hat{v}_{3,\text{red}}(t), \quad (16)$$

$$\hat{v}_{2,\text{blue}}(t) = \hat{v}_{2,\text{red}}(t), \quad (17)$$

$$\hat{v}_{3,\text{blue}}(t) = \hat{v}_{1,\text{red}}(t), \quad (18)$$

$$\hat{v}_{1,\text{green}}(t) = \hat{v}_{3,\text{green}}(t) = \hat{v}_{2,\text{red}}(t) = \hat{v}_{2,\text{blue}}(t), \quad (19)$$

and

$$\tau_1 = 2\tau_2 = \tau_3. \quad (20)$$

Equations (12 - 20) form a complete set of equations to describe the volume fraction evolution of each particle colour in each compartment of the ideal system. For the full derivation of the model, readers can refer to Appendix A.

The compartmental residence times are then determined by fitting the volume fractions measured from the DEM simulation to the ideal model and Figure 6 shows the results for the compartment z_1 . The results for the other compartments are determined in a similar manner and they are summarised in Table 2. The average value, $\tau_1 = 56$ s, is used for the compartmental population balance model. The values of τ_2 and τ_3 are determined according to Equation (20).

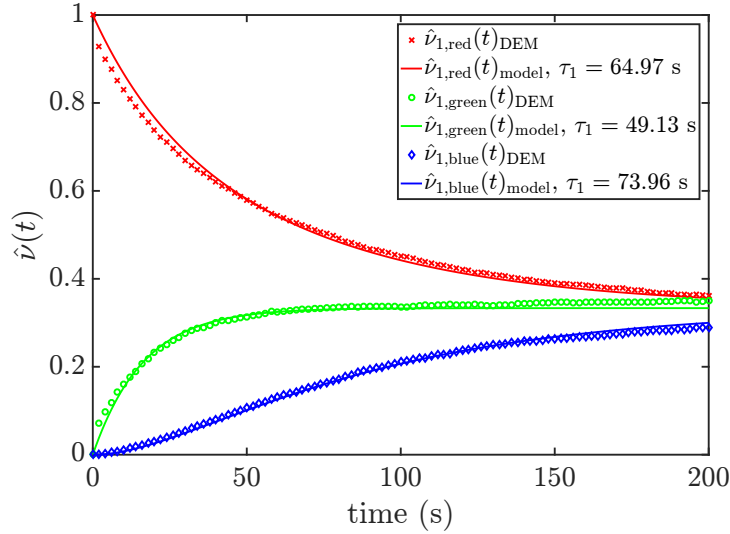


Figure 6: Ideal model fitted to the measured volume fractions in z_1 .

3.2 Collision rate function

Results presented in this section are obtained using the DEM simulation carried out with the experimental particle size distribution (Figure 3b). As mentioned in Section 2.2, DEM is used to determine a suitable collision rate function $C(d_i, d_j)$ for the population balance model. This is done by fitting the collision frequencies extracted from the DEM simulation to a list of known collision rate functions in the literature.

Table 2: *Fitted residence times.*

compartment, z	particle type, c	$\hat{v}_{z,c}(0)$	τ_1 (s)
1	red	1.0	64.97
1	green	0.0	49.13
1	blue	0.0	73.96
2	red	0.0	45.10
2	green	1.0	51.44
2	blue	0.0	60.52
3	red	0.0	70.61
3	green	0.0	33.09
3	blue	1.0	55.12
			$\bar{\tau}_1 \approx 56$

The collision frequency normalised by the number of particles in DEM is calculated as [24]:

$$C(d_i, d_j) = \frac{N_{\text{col}}(d_i, d_j)}{N_{\text{part}}(d_i)N_{\text{part}}(d_j)\Delta t}, \quad (21)$$

where $N_{\text{col}}(d_i, d_j)$ is the number of collisions between particles with the diameters d_i and d_j during the time interval Δt , and $N_{\text{part}}(d_i)$ is the number of particles with diameter d_i . In this case, particle-particle collisions are recorded over a period of 1 second and a total of 2.8×10^7 collisions are considered.

Table 3: *Collision rate functions in the literature. Assembled by [24].*

Name	Collision rate function
Size independent [7]	$C(d_i, d_j) = 1$
Equipartition of kinetic energy (EKE) [55]	$C(d_i, d_j) \propto (d_i + d_j)^2 \sqrt{\frac{1}{d_i^3} + \frac{1}{d_j^3}}$
Equipartition of translational momentum (ETM) [29]	$C(d_i, d_j) \propto (d_i + d_j)^2 \sqrt{\frac{1}{d_i^6} + \frac{1}{d_j^6}}$
Perikinetic or Brownian motion [24]	$C(d_i, d_j) \propto \frac{d_i + d_j}{d_i d_j}$
Orthokinetic or induced shear [24]	$C(d_i, d_j) \propto (d_i + d_j)^3$

Each of the rate functions in Table 3 is fitted to the frequencies calculated from DEM and the results are plotted in Figure 7. Figure 7a shows the collision frequencies in DEM calculated with Equation (21) and it can be observed that the majority of collisions in the simulation are between the large and small particles. Particles of similar sizes collide with each other much less frequently than with particles of different sizes, as shown by the drop in collision frequencies along the axis of symmetry. Figures 7b-7f show the collision

rate functions in Table 3 fitted to the normalised frequencies calculated from DEM. From these plots, the collision rate functions which show similar patterns are the EKE and ETM kernels (Figures 7c and 7d).

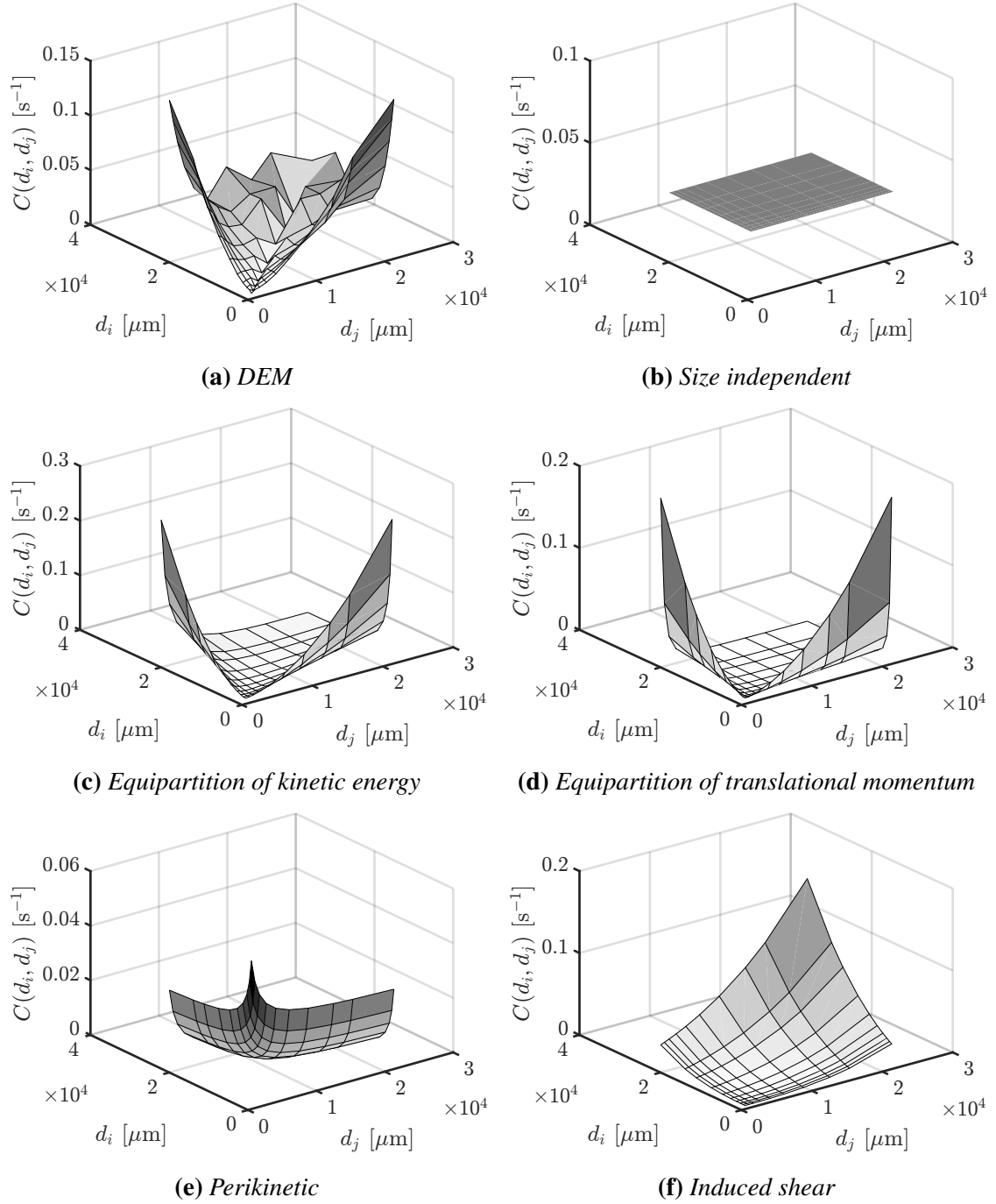


Figure 7: Normalised collision frequencies.

In order to decide between the EKE and ETM kernels, their relative errors with respect to the collision frequencies from DEM are compared. For each data point available, the

relative error is calculated as:

$$\epsilon_{\text{rel}}(d_i, d_j) = \frac{|C_{\text{DEM}}(d_i, d_j) - C_{\text{EKE/ETM}}(d_i, d_j)|}{C_{\text{DEM}}(d_i, d_j)}. \quad (22)$$

Figure 8 compares the relative errors for the EKE and ETM rate functions compared to the DEM extracted frequencies. The plots here show the point-by-point comparison between the DEM extracted frequencies in Figure 7a with the values in Figures 7c (EKE) and 7d (ETM). Based on the plots, it can be observed that the ETM rate function completely fails to predict the collision frequencies as the relative errors for most of the points exceed 1. For the EKE rate function, the average relative error over the points considered is 0.38. Considering that particles below 1 mm are ignored in the DEM simulation and the various idealised assumptions made in the EKE rate function, the overall fit of the EKE rate function to the collision frequencies from DEM can be considered excellent.

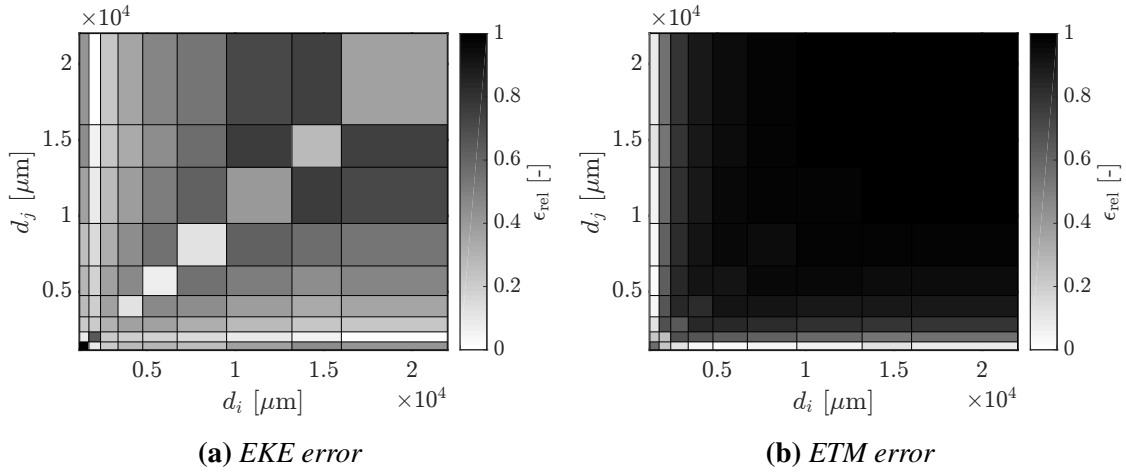


Figure 8: Relative error between the DEM extracted frequencies with the two closest collision rate functions - EKE and ETM.

4 Numerical method for the population balance model

As the population balance model is five-dimensional, the stochastic approach is the only viable method to solve it. There are two popular stochastic particle methods, which are the Direct Simulation Algorithm (DSA) and the Stochastic Weighted Algorithm (SWA) [35, 36, 40, 43, 46, 47, 51, 57]. In DSA, each computational particle represents the same number of particles whereas in SWA, each computational particle is tagged with a statistical weight which is proportional to the number of particles represented by the particle. As pointed out in [35, 36], DSA is unsuitable for compartmental models because of the high statistical noise observed, hence only SWA is used in this work.

For the population balance model described in Section 2, each compartment z is simulated with a system of stochastic particles:

$$Q_z(t) = (z, x_i, w_i), \quad i = 1, \dots, N_z(t), \quad (23)$$

where $z \in \mathbb{Z}$, $x_i \in \mathbb{X}$ and $w_i \in (0, w_{\max}]$ is the statistical weight. Each compartment z is scaled by a normalisation parameter n_z and it can be interpreted as the computational sample volume [36]. The number concentration of the particles of type x_i located in z is given by w_i/n_z .

The particle processes described in Section 2.2 are either implemented as jump processes or continuous processes. For this model, the jump processes include liquid addition, collision, breakage and particle transport, whereas the continuous processes include chemical reaction and penetration. In this section, the jump mechanisms and rates in the context of SWA for each of the particle processes are described, followed by the overall simulation algorithm.

4.1 Liquid addition

At the rate given by

$$R_{z, \text{droplet}} = \begin{cases} 3 \times \frac{n_z}{V_{\text{reactor}}} \frac{\dot{V}_1}{V_{\text{droplet}}} & , \text{ for } z = z_2, \\ 0 & , \text{ for } z = z_1, z_3, \end{cases} \quad (24)$$

liquid particles of the form $(z, x_{\text{droplet}}, 1)$ are introduced into the system. V_{reactor} is the volume of the mixer and the term n_z/V_{reactor} scales the rate according to the normalisation parameter.

4.2 Breakage

The total breakage jump rate in a compartment z is

$$R_{z, \text{break}} = \sum_{i=1}^{N_z(t)} r_{z, \text{break}}(x_i). \quad (25)$$

The index i of the particle to break within a compartment z is selected with probability

$$\frac{r_{z, \text{break}}(x_i)}{R_{z, \text{break}}}, \quad (26)$$

and the jump process takes the following form

$$(z, x_i, w_i) \rightarrow (z, y, \gamma_{\text{break}}(x_i, w_i, y)). \quad (27)$$

The fragment y takes the following forms with different probabilities:

$$\begin{aligned} y = x_j & \quad , \quad \text{with probability} = \frac{m(x_j)}{m(x_i)}, \\ y = x_i - x_j & \quad , \quad \text{with probability} = 1 - \frac{m(x_j)}{m(x_i)}. \end{aligned} \quad (28)$$

The breakage weight transfer function γ_{break} is defined to conserve total mass:

$$\gamma_{\text{break}}(x_i, w_i, y) = w_i \times \frac{m(x_i)}{m(y)}. \quad (29)$$

Full details regarding the breakage algorithm for weighted particles including its convergence properties can be found in [36].

4.3 Particle transport

At the rate

$$R_{z, \text{transport}} = \frac{N_z(t)}{\tau_z}, \quad (30)$$

a particle is uniformly selected in compartment z to undergo the following jump processes which depend on the initial location:

- $z = z_1$

$$(z_1, x_i, w_i) \rightarrow (z_2, x_i, w_i); \quad (31)$$

- $z = z_3$

$$(z_3, x_i, w_i) \rightarrow (z_2, x_i, w_i); \quad (32)$$

- $z = z_2$

$$\begin{aligned} (z_2, x_i, w_i) &\rightarrow (z_1, x_i, w_i), & \text{with probability} &= 0.5, \\ (z_2, x_i, w_i) &\rightarrow (z_3, x_i, w_i), & \text{with probability} &= 0.5. \end{aligned} \quad (33)$$

Full details regarding the implementation of particle transport in stochastic particle frameworks can be found in [35, 36, 41].

4.4 Collision

The outcome of a collision jump process depends on the coalescence efficiency \tilde{K} :

$$\begin{aligned} (x_i, w_i), (x_j, w_j) &\rightarrow (T_{\text{comp}}(x_i + x_j), \gamma_{\text{coal}}(x_i, w_i, x_j, w_j)), (x_j, w_j), & \text{if } \tilde{K}(x_i, x_j) = 1, \\ (x_i, w_i), (x_j, w_j) &\rightarrow (T_{\text{comp}}(x_i), w_i), (x_j, w_j), & \text{if } \tilde{K}(x_i, x_j) = 0. \end{aligned} \quad (34)$$

The second particle, x_j , is left unchanged in order to achieve the correct convergence properties for SWA [36, 40, 47]. The weight transfer function for coalescence γ_{coal} is defined to conserve total mass:

$$\gamma_{\text{coal}}(x_i, w_i, x_j, w_j) = w_i \frac{m(x_i)}{m(x_i) + m(x_j)}. \quad (35)$$

Other mathematically valid weight transfer functions are investigated in [47].

A key challenge in implementing the collision process is the efficient calculation of the total rate. The collision kernel for the particle pair (x_i, w_i) and (x_j, w_j) in the context of SWA is [47]:

$$\begin{aligned} K_{z, \text{SWA}}(x_i, w_i, x_j, w_j) &= K_z(x_i, x_j) w_j \\ &= \omega_{\text{impeller}} U_{\text{col}} k_{z, \text{col}} C(d_i, d_j) w_j. \end{aligned} \quad (36)$$

In order for the rate to be calculated efficiently, it is necessary for the kernel to be in the form:

$$\begin{aligned} K_{z, \text{SWA}}(x_i, w_i, x_j, w_j) &= h_1^{(1)}(x_i, w_i) h_2^{(1)}(x_j, w_j) + h_1^{(2)}(x_i, w_i) h_2^{(2)}(x_j, w_j) + \\ &\dots + h_1^{(n_h)}(x_i, w_i) h_2^{(n_h)}(x_j, w_j), \end{aligned} \quad (37)$$

so that its sum can be factorised as

$$\sum_{\substack{i \neq j \\ i, j=1 \\ i, j=2 \\ \dots \\ i, j=n_h}}^{N_z(t)} K_{z, \text{SWA}}(x_i, w_i, x_j, w_j) = \lambda_1^{(1)} \lambda_2^{(1)} - H^{(1)} + \lambda_1^{(2)} \lambda_2^{(2)} - H^{(2)} + \dots + \lambda_1^{(n_h)} \lambda_2^{(n_h)} - H^{(n_h)} \quad (38)$$

where λ and H are defined as

$$\lambda_l^{(k)} = \sum_{i=1}^{N_z(t)} h_l^{(k)}(x_i, w_i), \quad l = 1, 2, \quad k = 1, 2, \dots, n_h, \quad (39)$$

$$H^{(k)} = \sum_{i=1}^{N_z(t)} h_1^{(k)}(x_i, w_i) h_2^{(k)}(x_i, w_i), \quad k = 1, 2, \dots, n_h. \quad (40)$$

Note that the terms $H^{(k)}$ are subtracted from $\lambda_1^{(k)} \lambda_2^{(k)}$ to remove self-collisions. In this form, the quantities $h_l^{(k)}$ and $h_1^{(k)} h_2^{(k)}$ can be stored in a binary tree which enable rapid calculation of the sums $\lambda_l^{(k)}$ and $H^{(k)}$ [26, 47].

The selection of the particle pair (x_i, w_i) and (x_j, w_j) depends on Equation (38) which can be interpreted as the sum of n_h individual rate terms. So, with probability

$$\frac{\lambda_1^{(k)} \lambda_2^{(k)} - H^{(k)}}{\sum_{i \neq j}^{N_z(t)} K_{z, \text{SWA}}(x_i, w_i, x_j, w_j)}, \quad (41)$$

the index, i and j , of the colliding particles are chosen according to the respective probabilities

$$\frac{h_1^{(k)}(x_i, w_i)}{\lambda_1^{(k)}} \quad \text{and} \quad \frac{h_2^{(k)}(x_j, w_j)}{\lambda_2^{(k)}}, \quad \text{with } i \neq j. \quad (42)$$

It is determined in Section 3.2 that the EKE collision rate function is the most suitable rate function for the high-shear granulation system. Later in this paper, the results produced with the EKE rate function are compared with the results from the original collision submodel which uses the size independent rate function. The collision rate function only affects the rate and the collision jump mechanism (34) remains unchanged. Due to the fact that the rate functions have different forms, the calculations of the rates need to be treated separately and they are described in the following sections.

4.4.1 Size independent

For the size independent collision rate function, $C(d_i, d_j) = 1$, the kernel is:

$$K_{z, \text{SWA}}^{\text{SIK}}(x_i, w_i, x_j, w_j) = \omega_{\text{impeller}} U_{\text{col}} k_{z, \text{col}} w_j, \quad (43)$$

where the superscript ‘SIK’ denotes the size independent kernel.

The total collision jump rate in a compartment z is given by [47]:

$$\begin{aligned} R_{z, \text{col}}^{\text{SIK}} &= \frac{1}{n_z} \sum_{i \neq j}^{N_z(t)} K_{z, \text{SWA}}^{\text{SIK}}(x_i, w_i, x_j, w_j) \\ &= \frac{1}{n_z} \omega_{\text{impeller}} U_{\text{col}} k_{z, \text{col}} \left[\sum_{i=1}^{N_z(t)} 1 \sum_{j=1}^{N_z(t)} w_j - \sum_{i=1}^{N_z(t)} w_i \right]. \end{aligned} \quad (44)$$

Comparing Equation (44) to (38), we have $\lambda_1^{(1)} = \sum 1$ and $\lambda_2^{(1)} = \sum w_j$. Based on these expressions, the index i is to be selected uniformly regardless of the particle properties and the index j is selected with probability $w_j / \sum w_j$. The step (41) can be skipped because there is only one rate term for this kernel, i.e. $n_h = 1$.

4.4.2 Equipartition of kinetic energy (EKE)

The collision kernel using the EKE rate function is

$$K_{z, \text{SWA}}^{\text{EKE}}(x_i, w_i, x_j, w_j) = \omega_{\text{impeller}} U_{\text{col}} k_{z, \text{col}} (d_i + d_j)^2 \sqrt{\frac{1}{d_i^3} + \frac{1}{d_j^3}} w_j. \quad (45)$$

The calculation of the rate becomes complicated for this kernel due to its complex form. In order to calculate the exact rate, it is necessary to loop through each pair of particle and this is computationally expensive. Therefore, the majorant technique which provides computationally efficient implementations of the kernel K is applied [20, 25, 40, 47].

To arrive in the form shown by Equation (38), the kernel (45) is estimated by the majorant kernel:

$$\hat{K}_{z, \text{SWA}}^{\text{EKE}}(x_i, w_i, x_j, w_j) = k_{\text{maj}} \omega_{\text{impeller}} U_{\text{col}} k_{z, \text{col}} (d_i^2 + d_j^2) \left(\frac{1}{d_i^{1.5}} + \frac{1}{d_j^{1.5}} \right) w_j \quad (46)$$

such that $K \leq \hat{K}$ and $k_{\text{maj}} = 1.42$ is the majorant scaling factor required to maintain the inequality. The value of k_{maj} is calculated by determining the maximum point of the ratio K/\hat{K} and solving it such that the ratio equals to one. This ensures that the majorant kernel is as efficient as it could be.

The total majorant collision jump rate in compartment z can then be expressed as:

$$\begin{aligned}
\hat{R}_{z, \text{col}}^{\text{EKE}} &= \frac{1}{n_z} \sum_{i \neq j}^{N_z(t)} \hat{K}_{z, \text{SWA}}^{\text{EKE}}(x_i, w_i, x_j, w_j) \\
&= \frac{k_{\text{maj}} \omega_{\text{impeller}} U_{\text{col}} k_{z, \text{col}}}{n_z} \left\{ \left[\sum_{i=1}^{N(t)} d_i^{0.5} \sum_{j=1}^{N(t)} w_j - \sum_{i=1}^{N(t)} d_i^{0.5} w_i \right] \right. \\
&\quad + \left[\sum_{i=1}^{N(t)} d_i^2 \sum_{j=1}^{N(t)} d_j^{-1.5} w_j - \sum_{i=1}^{N(t)} d_i^{0.5} w_i \right] + \left[\sum_{i=1}^{N(t)} d_i^{-1.5} \sum_{j=1}^{N(t)} d_j^2 w_j - \sum_{i=1}^{N(t)} d_i^{0.5} w_i \right] \\
&\quad \left. + \left[\sum_{i=1}^{N(t)} 1 \sum_{j=1}^{N(t)} d_j^{0.5} w_j - \sum_{i=1}^{N(t)} d_i^{0.5} w_i \right] \right\}. \tag{47}
\end{aligned}$$

Note that the term $\sum d_i^{0.5} w_i$ is subtracted from the terms to exclude self-collisions. The particle selection properties and the partial sums for this majorant kernel are summarised in Table 4.

Table 4: Particle selection properties based on Equation (47).

k	Equation	$\lambda_1^{(k)}$	$\lambda_2^{(k)}$	$h_1^{(k)}(x_i, w_i)$	$h_2^{(k)}(x_j, w_j)$
1	$\left[\sum d_i^{0.5} \sum w_j - \sum d_i^{0.5} w_i \right]$	$\sum d_i^{0.5}$	$\sum w_j$	$d_i^{0.5}$	w_j
2	$\left[\sum d_i^2 \sum d_j^{-1.5} w_j - \sum d_i^{0.5} w_i \right]$	$\sum d_i^2$	$\sum d_j^{-1.5} w_j$	d_i^2	$d_j^{-1.5} w_j$
3	$\left[\sum d_i^{-1.5} \sum d_j^2 w_j - \sum d_i^{0.5} w_i \right]$	$\sum d_i^{-1.5}$	$\sum d_j^2 w_j$	$d_i^{-1.5}$	$d_j^2 w_j$
4	$\left[\sum 1 \sum d_j^{0.5} w_j - \sum d_i^{0.5} w_i \right]$	$\sum 1$	$\sum d_j^{0.5} w_j$	1	$d_j^{0.5} w_j$

When a majorant kernel is used, it is necessary to introduce fictitious jumps in order to achieve the correct convergence properties [25]. Once the colliding pair (x_i, w_i) and (x_j, w_j) in a compartment z is chosen according to the selection properties in Table 4, the collision jump process (34) is performed with probability

$$\frac{K_{z, \text{SWA}}^{\text{EKE}}(x_i, w_i, x_j, w_j)}{\hat{K}_{z, \text{SWA}}^{\text{EKE}}(x_i, w_i, x_j, w_j)}, \tag{48}$$

otherwise the jump is fictitious, i.e. nothing happens in this step but time moves forward.

4.5 Simulation algorithm

The waiting time t_{wait} is generated from an exponential distribution [25]

$$\text{Prob}\{t_{\text{wait}} \geq s\} = \exp(-R_{\text{total}} s), \quad s \geq 0, \tag{49}$$

with the parameter

$$R_{\text{total}} = \sum_{z=\mathbb{Z}} [R_{z, \text{droplet}} + R_{z, \text{break}} + R_{z, \text{transport}} + R_{z, \text{col}}]. \tag{50}$$

A particle process (inception, breakage, transport, or collision) in a compartment z is chosen according to the probabilities

$$\frac{R_{z, \text{droplet}}}{R_{\text{total}}}, \quad \frac{R_{z, \text{break}}}{R_{\text{total}}}, \quad \frac{R_{z, \text{transport}}}{R_{\text{total}}}, \quad \frac{R_{z, \text{col}}}{R_{\text{total}}}.$$

$R_{z, \text{droplet}}$, $R_{z, \text{break}}$ and $R_{z, \text{transport}}$ are given by Equations (24), (25), and (30). $R_{z, \text{col}}$ is defined by Equations (44) or (47) depending on which collision rate function is used. Since there are three compartments, there are 12 jump processes considered in total. Once a particle process in a specific compartment is selected, the respective jump mechanisms described in Sections 4.1 - 4.4 are performed.

In between jump processes, the components of the particles change according to the following system of ordinary differential equations using the Linear Process Deferment Algorithm [45]:

$$\begin{aligned} \frac{ds_o}{dt} &= 0, & \frac{ds_r}{dt} &= r_{\text{reac}}(x), \\ \frac{dl_e}{dt} &= -r_{\text{reac}}(x) - r_{\text{pen}}(x), & \frac{dl_i}{dt} &= -r_{\text{reac}}(x) + r_{\text{pen}}(x), & \frac{dp}{dt} &= -r_{\text{reac}}(x). \end{aligned}$$

5 Application

The population balance model is simulated as closely as possible to a set of experimental conditions chosen from [34, Experiment B1]. The experimental conditions and several key model parameters are listed in Table 5. For the purpose of validating the population balance model, measurements of particle size distribution [34] and porosities [52] are available from the same set of experimental conditions.

The ability of the population balance model to predict the experimental measurements is investigated in this section, in particular the difference observed when the EKE collision kernel is applied as opposed to the size independent kernel. Here, the rate parameters described in Section 2.2 are optimised to fit the simulated responses to the experimental measurements using the software MoDS (Model Development Suite) [16]. The model contains five rate parameters ($k_{z, \text{break}}$, $k_{z, \text{reac}}$, $k_{z, \text{pen}}$, $k_{z, \text{col}}$, and $k_{z, \text{comp}}$) which are allowed to vary between different compartments. By assuming the rates of the particle processes are the same in z_1 and z_3 , there are $2 \times 5 = 10$ parameters to consider. This assumption also conforms to the symmetrical geometry of the mixer (Figure 1).

For each model evaluation, the compartments are initialised with a set of non-porous particles of the form:

$$x = (s_o, 0, 0, 0, 0)$$

following the measured size distribution of the initial lactose powder ($\mu_{\text{psd}} = 38.93 \mu\text{m}$, $\sigma_{\text{psd}} = 1.6 \mu\text{m}$). Once the solid particles are initialised, liquid droplets are added at the rate defined by Equation (24) and stopped after 120 seconds. The simulation is then allowed to continue for 300 seconds after the liquid addition phase and this refers to the wet massing

time in Table 5. Each model evaluation consists of a number of independent stochastic runs and the results are averaged over the runs.

The quality of the stochastic simulations depends on the number of computational particles and the number of stochastic runs at the expense of CPU time. In a preliminary convergence test, it is determined that 2000 particles per compartment and 8 stochastic runs are sufficient to achieve convergence for this system. Using these numbers, a model evaluation takes about a few minutes when the size independent kernel is used and about an hour when the EKE kernel is used.

Table 5: *Model physical parameters.*

Description	Symbol	Value
<i>Known process settings</i>		
Material density	ρ_{s_0}	1545.0 kg/m ³
Binder density	ρ_{l_e}	998.0 kg/m ³
Binder viscosity	η	1.0×10^{-3} Pa s
Reactor volume	V_{reactor}	3.0×10^{-3} m ³
Impeller speed	ω_{impeller}	2 rev/s
Binder flow rate	\dot{V}_l	1.25×10^{-6} m ³ /s
Wet massing time	-	300 s
Binder to powder ratio	-	150 ml:1000 g
<i>Model parameters – approximated</i>		
Powder size distribution; location	μ_{psd}	38.93 μm
Powder size distribution; shape	σ_{psd}	1.6 μm
Droplet volume	V_{droplet}	1.80×10^{-13} m ³
Particle-particle collision velocity	U_{col}	9.11×10^{-2} m/s
Minimum particle porosity after compaction	ϵ_{min}	0.25
Breakage; minimum fragment volume	$v_{\text{frag,min}}$	5.236×10^{-13} m ³
Breakage; particle-impeller impact velocity	U_{imp}	0.82 m/s

To quantify the agreement between the model and experiment, the sum of squares objective function is used:

$$OF = \sum_{i=1}^Y (y_i^{\text{sim}} - y_i^{\text{exp}})^2, \quad (51)$$

where y^{sim} denotes the model response, y^{exp} denotes the experimental response and Y is the total number of responses.

Optimisation of the objective function is carried out in two stages. The first stage involves a quasi-random global search using a Sobol low-discrepancy sequence [54]. This is followed by a local optimisation starting from the best point using the Hooke and Jeeves' algorithm [28].

The objective function includes a particle size distribution and also particle porosities. The particle size distribution is represented by mass fractions, f_m , of 19 size classes. On the

other hand, only porosities for 15 particle size classes are included in the objective function as opposed to 19 due to limitations of the experimental measurements. Considering both sets of data, there are 34 observation points in total.

In order to study the effects of implementing the EKE kernel, two versions of the population balance model which differ in the collision kernel (EKE and size independent) are investigated. The optimisation of the objective function is carried out for both models and the optimised rate parameters are shown in Tables 6 and 7. For both models, a total of 10,000 Sobol evaluations and a few hundred additional evaluations for the local optimisation are performed to arrive at the optimised rate parameters.

Figures 9 and 10 show the best fit size distribution and porosities respectively from the population balance model. Looking closely at Figure 9, it can be observed that the EKE kernel is able to describe the process more accurately as the generated size distribution is much closer to the experimental data. By using the EKE kernel, the model is able to generate a wider range of particle sizes compared to the size independent kernel.

As for the porosities (Figure 10), the value 0 is given when there are no particles of that size. Similar to the size distribution, the values generated with the EKE kernel are also much closer to the experimental data partly because the model is not able to generate any particles above 850 μm when the size independent kernel is used. Looking at the size dependency of the porosities, the experimental data suggest that the porosities should increase with size but an opposite trend is exhibited by the larger particles. This is partly because the kernel favours collisions of the very large particles and this leads to higher compaction rates for the larger particles.

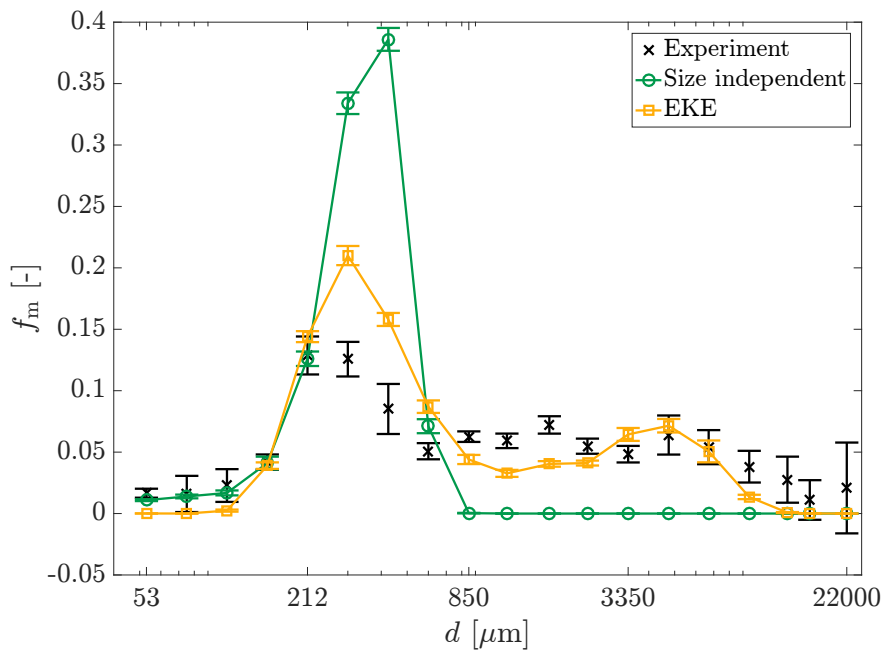


Figure 9: Best fit particle size distributions.

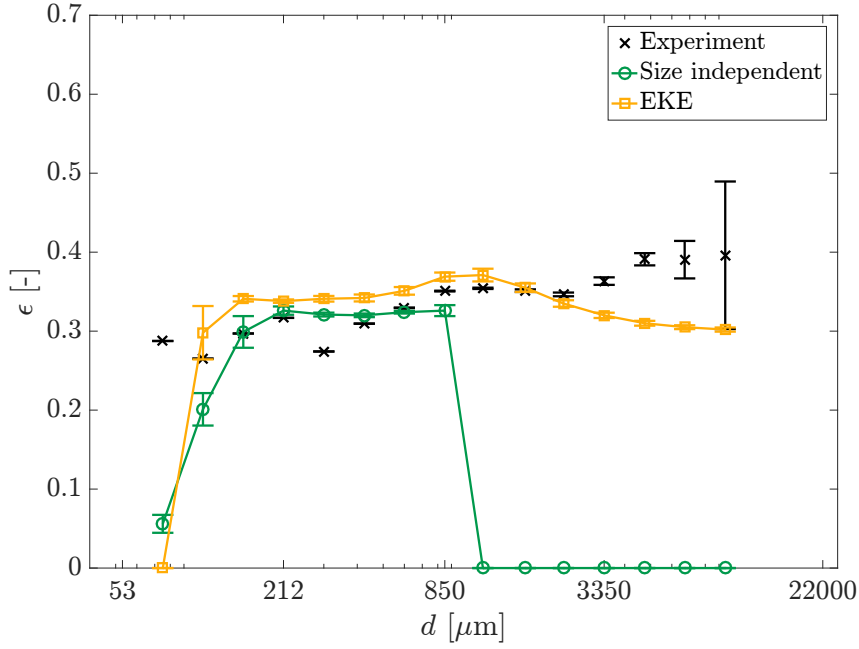


Figure 10: Best fit porosity distributions.

Table 6: Optimised rate parameters when the size independent kernel is used.

Rate parameter	Units	z_1/z_3	z_2
$k_{z, \text{break}}$	s m^{-5}	1.04×10^4	2.68×10^6
$k_{z, \text{reac}}$	m s^{-1}	3.42×10^{-16}	1.41×10^{-14}
$k_{z, \text{pen}}$	$\text{kg}^{0.5} \text{s}^{-1.5} \text{m}^{-3.5}$	8.61×10^2	1.89×10^2
$k_{z, \text{col}}$	m^3	3.50×10^{-17}	2.27×10^{-13}
$k_{z, \text{comp}}$	-	8.55×10^{-1}	7.57×10^{-1}

Table 7: Optimised rate parameters when the EKE kernel is used.

Rate parameter	Units	z_1/z_3	z_2
$k_{z, \text{break}}$	s m^{-5}	5.18×10^{10}	3.56×10^3
$k_{z, \text{reac}}$	m s^{-1}	1.21×10^{-16}	2.10×10^{-14}
$k_{z, \text{pen}}$	$\text{kg}^{0.5} \text{s}^{-1.5} \text{m}^{-3.5}$	8.85×10^3	1.22×10^1
$k_{z, \text{col}}$	m^3	7.60×10^{-15}	2.77×10^{-9}
$k_{z, \text{comp}}$	-	1.00×10^0	3.61×10^{-1}

6 Conclusions

This paper presents how DEM simulations can be coupled to a population balance model to model a batch granulation process. As both approaches have different capabilities, they are used to complement each other in this work.

DEM is used to analyse flow patterns in the mixer and the simulations reveal two crucial findings. First, it is found that segregation of particles is inherent especially in the axial direction and this justifies the usage of multiple compartments in the population balance model. Second, the results suggest that the collision frequencies between particles are size dependent and this should be reflected in the population balance model. Even though DEM is able to provide detailed information regarding the movement of particles, it is computationally expensive and unsuitable for long time scale studies.

On the other hand, population balance models are computationally cheap. However, they often require some prior knowledge of the system. For example, the residence times of the multi-compartment model and the rate of collision between particles are unknown. Hence, methodologies are developed to determine the compartmental residence times and also a suitable collision rate function for the population balance model from DEM.

Based on the particle-particle collision frequencies extracted from DEM, it is determined that the EKE kernel is the most appropriate kernel to use in the population balance model. In order to use it in a stochastic particle framework, the majorant technique is adapted to this kernel to enable rapid calculation of the collision rate. Then, the results generated with this kernel are compared to the results produced with the size independent kernel. By using the EKE kernel, we find that the agreement between the simulated results and the experimental data is significantly improved.

Despite the improvement observed, there are noticeable weaknesses in the model especially in predicting the properties of the larger particles. Hence, an immediate future work will involve a detailed sensitivity analysis to decompose the effects of the model parameters on the model responses. This should reveal further insights on the behaviour of the model.

Acknowledgements

This project is partly funded by the National Research Foundation (NRF), Prime Minister's Office, Singapore under its Campus for Research Excellence and Technological Enterprise (CREATE) Programme.

References

- [1] D. Barrasso and R. Ramachandran. Multi-scale modeling of granulation processes: Bi-directional coupling of PBM with DEM via collision frequencies. *Chemical En-*

Engineering Research and Design, 2014. doi:10.1016/j.cherd.2014.04.016.

- [2] D. Barrasso, A. Tamrakar, and R. Ramachandran. A reduced order PBM-ANN model of a multi-scale PBM-DEM description of a wet granulation process. *Chemical Engineering Science*, 119(0):319–329, 2014. doi:10.1016/j.ces.2014.08.005.
- [3] D. Barrasso, T. Eppinger, F. E. Pereira, R. Aglave, K. Debus, S. K. Bermingham, and R. Ramachandran. A multi-scale, mechanistic model of a wet granulation process using a novel bi-directional PBM-DEM coupling algorithm. *Chemical Engineering Science*, 123(0):500–513, 2015. doi:10.1016/j.ces.2014.11.011.
- [4] R. Boerefijn, Z. Ning, and M. Ghadiri. Disintegration of weak lactose agglomerates for inhalation applications. *International Journal of Pharmaceutics*, 172(1-2):199–209, 1998. doi:10.1016/S0378-5173(98)00207-5.
- [5] J. Bouffard, F. Bertrand, and J. Chaouki. A multiscale model for the simulation of granulation in rotor-based equipment. *Chemical Engineering Science*, 81:106–117, 2012. doi:10.1016/j.ces.2012.06.025.
- [6] A. Braumann and M. Kraft. Incorporating experimental uncertainties into multivariate granulation modelling. *Chemical Engineering Science*, 65(3):1088–1100, 2010. doi:10.1016/j.ces.2009.09.063.
- [7] A. Braumann, M. J. Goodson, M. Kraft, and P. R. Mort. Modelling and validation of granulation with heterogeneous binder dispersion and chemical reaction. *Chemical Engineering Science*, 62(17):4717–4728, 2007. doi:10.1016/j.ces.2007.05.028.
- [8] A. Braumann, M. Kraft, and P. R. Mort. Parameter estimation in a multidimensional granulation model. *Powder Technology*, 197(3):196–210, 2010. doi:10.1016/j.powtec.2009.09.014.
- [9] A. Braumann, M. Kraft, and W. Wagner. Numerical study of a stochastic particle algorithm solving a multidimensional population balance model for high shear granulation. *Journal of Computational Physics*, 229(20):7672–7691, 2010. doi:10.1016/j.jcp.2010.06.021.
- [10] A. Braumann, P. L. W. Man, and M. Kraft. Statistical approximation of the inverse problem in multivariate population balance modeling. *Industrial & Engineering Chemistry Research*, 49(1):428–438, 2010. doi:10.1021/ie901230u.
- [11] A. Braumann, P. L. W. Man, and M. Kraft. The inverse problem in granulation modeling—two different statistical approaches. *AIChE Journal*, 57(11):3105–3121, 2011. doi:10.1002/aic.12526.
- [12] C. Broadbent, J. Bridgwater, and D. Parker. The effect of fill level on powder mixer performance using a positron camera. *The Chemical Engineering Journal and the Biochemical Engineering Journal*, 56(3):119–125, 1995. doi:10.1016/0923-0467(94)02906-7.

- [13] I. Cameron, F. Wang, C. Immanuel, and F. Stepanek. Process systems modelling and applications in granulation: A review. *Chemical Engineering Science*, 60(14):3723–3750, 2005. doi:10.1016/j.ces.2005.02.004. Granulation across the length scales - 2nd International Workshop on Granulation.
- [14] A. Chaudhury, H. Wu, M. Khan, and R. Ramachandran. A mechanistic population balance model for granulation processes: Effect of process and formulation parameters. *Chemical Engineering Science*, 107:76–92, 2014. doi:10.1016/j.ces.2013.11.031.
- [15] A. Chaudhury, M. E. Armenante, and R. Ramachandran. Compartment based population balance modeling of a high shear wet granulation process using data analytics. *Chemical Engineering Research and Design*, 95(0):211–228, 2015. doi:10.1016/j.cherd.2014.10.024.
- [16] CMCL Innovations. MoDS (Model Development Suite), 2015. URL <http://www.cmclinnovations.com/mods/>. Date accessed: 12.01.2015.
- [17] B. Crüger, V. Salikov, S. Heinrich, S. Antonyuk, V. Sutkar, N. Deen, and J. Kuipers. Coefficient of restitution for particles impacting on wet surfaces: An improved experimental approach. *Particuology*, 25:1–9, 2016. doi:10.1016/j.partic.2015.04.002.
- [18] A. Darelius, H. Brage, A. Rasmuson, I. N. Björn, and S. Folestad. A volume-based multi-dimensional population balance approach for modelling high shear granulation. *Chemical Engineering Science*, 61(8):2482–2493, 2006. doi:10.1016/j.ces.2005.11.016.
- [19] M. Dosta, S. Antonyuk, and S. Heinrich. Multiscale simulation of the fluidized bed granulation process. *Chemical Engineering & Technology*, 35(8):1373–1380, 2012. doi:10.1002/ceat.201200075.
- [20] A. Eibeck and W. Wagner. Approximative solution of the coagulation–fragmentation equation by stochastic particle systems. *Stochastic analysis and applications*, 18(6): 921–948, 2000. doi:10.1080/07362990008809704.
- [21] B. J. Ennis, G. Tardos, and R. Pfeffer. A microlevel-based characterization of granulation phenomena. *Powder Technology*, 65(1-3):257–272, 1991. doi:10.1016/0032-5910(91)80189-P. A Special Volume Devoted to the Second Symposium on Advances in Particulate Technology.
- [22] A. Faure, P. York, and R. Rowe. Process control and scale-up of pharmaceutical wet granulation processes: a review. *European Journal of Pharmaceutics and Biopharmaceutics*, 52(3):269–277, 2001. doi:10.1016/S0939-6411(01)00184-9.
- [23] B. Freireich, J. Li, J. Litster, and C. Wassgren. Incorporating particle flow information from discrete element simulations in population balance models of mixer-coaters. *Chemical Engineering Science*, 66(16):3592–3604, 2011. doi:10.1016/j.ces.2011.04.015.

- [24] J. A. Gantt, I. T. Cameron, J. D. Litster, and E. P. Gatzke. Determination of coalescence kernels for high-shear granulation using DEM simulations. *Powder Technology*, 170(2):53–63, 2006. doi:10.1016/j.powtec.2006.08.002.
- [25] M. Goodson and M. Kraft. An efficient stochastic algorithm for simulating nanoparticle dynamics. *Journal of Computational Physics*, 183(1):210–232, 2002. doi:10.1006/jcph.2002.7192.
- [26] M. Goodson and M. Kraft. Simulation of coalescence and breakage: an assessment of two stochastic methods suitable for simulating liquid-liquid extraction. *Chemical Engineering Science*, 59(18):3865–3881, 2004. doi:10.1016/j.ces.2004.05.029.
- [27] S. Heinrich, M. Dosta, and S. Antonyuk. Chapter two - multiscale analysis of a coating process in a wurster fluidized bed apparatus. In G. B. Marin and J. Li, editors, *Mesoscale Modeling in Chemical Engineering Part I*, volume 46 of *Advances in Chemical Engineering*, pages 83 – 135. Academic Press, 2015. doi:10.1016/bs.ache.2015.10.012.
- [28] R. Hooke and T. A. Jeeves. “Direct Search” solution of numerical and statistical problems. *Journal of the ACM*, 8(2):212–229, 1961. doi:10.1145/321062.321069.
- [29] M. Hounslow. The population balance as a tool for understanding particle rate processes. *KONA Powder and Particle Journal*, 16:179–193, 1998. doi:10.14356/kona.1998021.
- [30] S. M. Iveson. Limitations of one-dimensional population balance models of wet granulation processes. *Powder Technology*, 124(3):219–229, 2002. doi:10.1016/S0032-5910(02)00026-8. Control of Particulate Processes IV.
- [31] S. M. Iveson, J. D. Litster, K. Hapgood, and B. J. Ennis. Nucleation, growth and breakage phenomena in agitated wet granulation processes: a review. *Powder Technology*, 117(1-2):3–39, 2001. doi:10.1016/S0032-5910(01)00313-8. Granulation and Coating of Fine Powders.
- [32] J. Jones and J. Bridgwater. A case study of particle mixing in a ploughshare mixer using positron emission particle tracking. *International Journal of Mineral Processing*, 53(1):29–38, 1998. doi:10.1016/S0301-7516(97)00054-9.
- [33] J. Jones, D. Parker, and J. Bridgwater. Axial mixing in a ploughshare mixer. *Powder Technology*, 178(2):73–86, 2007. doi:10.1016/j.powtec.2007.04.006.
- [34] C. A. Kastner, G. P. Brownbridge, S. Mosbach, and M. Kraft. Impact of powder characteristics on a particle granulation model. *Chemical Engineering Science*, 97(0):282–295, 2013. doi:10.1016/j.ces.2013.04.032.
- [35] K. F. Lee, S. Mosbach, M. Kraft, and W. Wagner. A multi-compartment population balance model for high shear granulation. *Computers & Chemical Engineering*, 75:1–13, 2015. doi:10.1016/j.compchemeng.2015.01.009.

- [36] K. F. Lee, R. I. Patterson, W. Wagner, and M. Kraft. Stochastic weighted particle methods for population balance equations with coagulation, fragmentation and spatial inhomogeneity. *Journal of Computational Physics*, 303:1–18, 2015. doi:10.1016/j.jcp.2015.09.031.
- [37] J. Li, B. Freireich, C. Wassgren, and J. D. Litster. A general compartment-based population balance model for particle coating and layered granulation. *AIChE Journal*, 58(5):1397–1408, 2012. doi:10.1002/aic.12678.
- [38] L. X. Liu and J. D. Litster. Population balance modelling of granulation with a physically based coalescence kernel. *Chemical Engineering Science*, 57(12):2183–2191, 2002. doi:10.1016/S0009-2509(02)00110-0. Population balance modelling of particulate systems.
- [39] C. L. Marshall Jr., P. Rajniak, and T. Matsoukas. Multi-component population balance modeling of granulation with continuous addition of binder. *Powder Technology*, 236:211–220, 2013. doi:10.1016/j.powtec.2012.01.027. Special Issue: Pharmaceutical Powders.
- [40] W. J. Menz, R. I. Patterson, W. Wagner, and M. Kraft. Application of stochastic weighted algorithms to a multidimensional silica particle model. *Journal of Computational Physics*, 248(0):221–234, 2013. doi:10.1016/j.jcp.2013.04.010.
- [41] W. J. Menz, J. Akroyd, and M. Kraft. Stochastic solution of population balance equations for reactor networks. *Journal of Computational Physics*, 256(0):615–629, 2014. doi:10.1016/j.jcp.2013.09.021.
- [42] J. N. Michaels. Toward rational design of powder processes. *Powder Technology*, 138(1):1–6, 2003. doi:10.1016/j.powtec.2003.08.035. World Congress of Particle Technology.
- [43] J. R. Norris. Smoluchowski’s coagulation equation: uniqueness, nonuniqueness and a hydrodynamic limit for the stochastic coalescent. *The Annals of Applied Probability*, 9(1):78–109, 1999. doi:10.1214/aoap/1029962598.
- [44] M. Oullion, G. Reynolds, and M. Hounslow. Simulating the early stage of high-shear granulation using a two-dimensional monte-carlo approach. *Chemical Engineering Science*, 64(4):673 – 685, 2009. doi:10.1016/j.ces.2008.08.014. 3rd International Conference on Population Balance Modelling.
- [45] R. Patterson, J. Singh, M. Balthasar, M. Kraft, and J. Norris. The Linear Process Deferral Algorithm: A new technique for solving population balance equations. *SIAM Journal on Scientific Computing*, 28(1):303–320, 2006. doi:10.1137/040618953.
- [46] R. I. Patterson and W. Wagner. A stochastic weighted particle method for coagulation–advection problems. *SIAM Journal on Scientific Computing*, 34(3): B290–B311, 2012. doi:10.1137/110843319.

- [47] R. I. Patterson, W. Wagner, and M. Kraft. Stochastic weighted particle methods for population balance equations. *Journal of Computational Physics*, 230(19):7456 – 7472, 2011. doi:10.1016/j.jcp.2011.06.011.
- [48] J. M.-H. Poon, C. D. Immanuel, F. J. Doyle, III, and J. D. Litster. A three-dimensional population balance model of granulation with a mechanistic representation of the nucleation and aggregation phenomena. *Chemical Engineering Science*, 63(5):1315 – 1329, 2008. doi:10.1016/j.ces.2007.07.048. Control of Particulate Processes.
- [49] R. Ramachandran, C. D. Immanuel, F. Stepanek, J. D. Litster, and F. J. D. III. A mechanistic model for breakage in population balances of granulation: Theoretical kernel development and experimental validation. *Chemical Engineering Research and Design*, 87(4):598 – 614, 2009. doi:10.1016/j.cherd.2008.11.007. 13th European Conference on Mixing: New developments towards more efficient and sustainable operations.
- [50] G. Reynolds, C. Biggs, A. Salman, and M. Hounslow. Non-uniformity of binder distribution in high-shear granulation. *Powder Technology*, 140(3):203 – 208, 2004. doi:10.1016/j.powtec.2004.01.017. 1st International Workshop on Granulation (Granulation across the length scales: linking microscopic experiments and models to real process operation).
- [51] S. Rjasanow and W. Wagner. A stochastic weighted particle method for the boltzmann equation. *Journal of Computational Physics*, 124(2):243–253, 1996. doi:10.1006/jcph.1996.0057.
- [52] J.-G. Rosenboom, S. Antonyuk, S. Heinrich, and M. Kraft. Characterisation of lactose powder and granules for multivariate wet granulation modelling. *Chemical Engineering Science*, 123:395 – 405, 2015. doi:10.1016/j.ces.2014.11.013.
- [53] M. Sen and R. Ramachandran. A multi-dimensional population balance model approach to continuous powder mixing processes. *Advanced Powder Technology*, 24(1):51 – 59, 2013. doi:10.1016/j.appt.2012.02.001.
- [54] I. M. Sobol. On the systematic search in a hypercube. *SIAM Journal on Numerical Analysis*, 16(5):790–793, 1979. URL <http://www.jstor.org/stable/2156633>.
- [55] H. Tan, M. Goldschmidt, R. Boerefijn, M. Hounslow, A. Salman, and J. Kuipers. Building population balance model for fluidized bed melt granulation: lessons from kinetic theory of granular flow. *Powder Technology*, 142(2-3):103 – 109, 2004. doi:10.1016/j.powtec.2004.04.030.
- [56] J. G. Zadow. Lactose: Properties and uses. *Journal of Dairy Science*, 67(11):2654–2679, 1984. doi:10.3168/jds.S0022-0302(84)81625-2.
- [57] H. Zhao, F. E. Kruis, and C. Zheng. A differentially weighted Monte Carlo method for two-component coagulation. *Journal of Computational Physics*, 229(19):6931 – 6945, 2010. doi:10.1016/j.jcp.2010.05.031.

A Derivation of three compartment mixing model

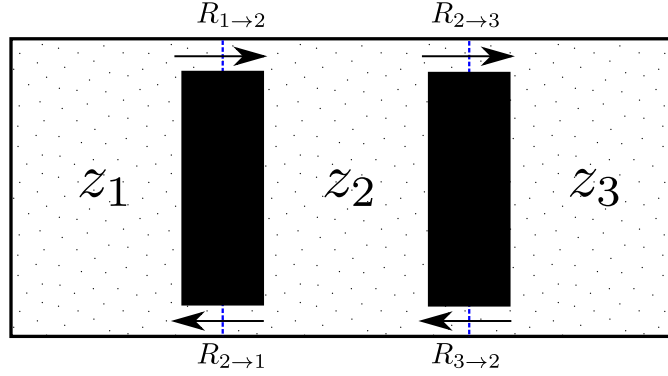


Figure 11: *Idealised compartmental mixer in which particles travel at a constant rate through pre-defined channels. Each compartment acts as a well-mixed CSTR.*

A model for each particle volume fraction evolution in each compartment is derived by considering an idealised reactor system as shown in Figure 11. Here, a tertiary particle colour system is initially loaded as [red, green, blue] and each compartment is perfectly mixed. Such a construction assumes that the separation between compartment boundaries is sufficiently large and the time step between analysis frames is sufficiently small such that particles cannot ‘skip’ over compartments (e.g. from C_1 directly to C_3). The volume flow rate from compartment k to p can then be written as the sum of the time-dependent component volume flow-rates $Q_{k \rightarrow p}^{[j]}(t)$ as:

$$Q_{k \rightarrow p} = Q_{k \rightarrow p}^{[\text{red}]}(t) + Q_{k \rightarrow p}^{[\text{green}]}(t) + Q_{k \rightarrow p}^{[\text{blue}]}(t). \quad (\text{A.1})$$

Since the mixer is being operated at a constant speed we expect the volume transfer rate (driven by the energy supplied by the motor) to be constant with respect to time (neglecting the time taken to establish any potential particle flow channels). Assuming constant volume hold-up within each compartment (no net movement between compartments was observed during the experiment) it follows that, for compartments connected to a single other compartment (compartment 1 and 3 in Figure 11),

$$Q_{k \rightarrow p} = Q_{p \rightarrow k}. \quad (\text{A.2})$$

Furthermore, mixer symmetry dictates that:

$$Q_{1 \rightarrow 2} = Q_{3 \rightarrow 2}, \quad (\text{A.3})$$

and thus:

$$Q_{1 \rightarrow 2} = Q_{2 \rightarrow 1} = Q_{2 \rightarrow 3} = Q_{3 \rightarrow 2}. \quad (\text{A.4})$$

If particles have a uniform density across the system then the corresponding mass flow rates \dot{M} may be written as:

$$\dot{M}_{1 \rightarrow 2} = \dot{M}_{2 \rightarrow 1} = \dot{M}_{2 \rightarrow 3} = \dot{M}_{3 \rightarrow 2}. \quad (\text{A.5})$$

By definition the average residence time τ of a compartment is given by:

$$\tau_i = \frac{V_{i,T}}{Q_{i,out}}, \quad (\text{A.6})$$

where $V_{i,T}$ and $Q_{i,out}$ are the total particle volume and volumetric flow-rate out of compartment i , respectively. The compartments are defined such that $V_{1,T} = V_{2,T} = V_{3,T}$ and $Q_{1,out} = Q_{2,out}/2 = Q_{3,out}$, and so:

$$\tau_1 = 2\tau_2 = \tau_3. \quad (\text{A.7})$$

Again, assuming constant particle density, a dynamic component balance over the red particles in C_1 may be written as:

$$\frac{dV_{1,\text{red}}(t)}{dt} = Q_{2 \rightarrow 1}^{[\text{red}]} - Q_{1 \rightarrow 2}^{[\text{red}]} \quad (\text{A.8})$$

If half of the red particles in C_2 are assumed to exit into C_1 and half through to C_3 (again this assumes that C_2 is well mixed) then it follows from (A.8) that:

$$\begin{aligned} V_{1,T} \frac{d\hat{v}_{1,\text{red}}(t)}{dt} &= \frac{V_{2,\text{red}}}{2\tau_2} - \frac{V_{1,\text{red}}}{\tau_1} \\ \rightarrow \frac{d\hat{v}_{1,\text{red}}(t)}{dt} &= \frac{1}{\tau_1} (\hat{v}_{2,\text{red}}(t) - \hat{v}_{1,\text{red}}(t)). \end{aligned} \quad (\text{A.9})$$

A similar argument applied to C_2 and C_3 yields:

$$\frac{d\hat{v}_{2,\text{red}}(t)}{dt} = \frac{1}{\tau_1} (\hat{v}_{1,\text{red}}(t) + \hat{v}_{3,\text{red}}(t) - 2\hat{v}_{2,\text{red}}(t)), \quad (\text{A.10})$$

$$\frac{d\hat{v}_{3,\text{red}}(t)}{dt} = \frac{1}{\tau_1} (\hat{v}_{2,\text{red}}(t) - \hat{v}_{3,\text{red}}(t)). \quad (\text{A.11})$$

Equations (A.9), (A.10) and (A.11) form a system of ordinary differential equations with initial conditions $\hat{v}_{1,\text{red}}(0) = 1$ and $\hat{v}_{2,\text{red}}(0) = \hat{v}_{3,\text{red}}(0) = 0$. The solutions to the system are then:

$$\hat{v}_{1,\text{red}}(t) = \frac{1}{2} \exp\left(-\frac{t}{\tau_1}\right) + \frac{1}{6} \exp\left(-\frac{3t}{\tau_1}\right) + \frac{1}{3}, \quad (\text{A.12})$$

$$\hat{v}_{2,\text{red}}(t) = -\frac{1}{3} \exp\left(-\frac{3t}{\tau_1}\right) + \frac{1}{3}, \quad (\text{A.13})$$

$$\hat{v}_{3,\text{red}}(t) = -\frac{1}{2} \exp\left(-\frac{t}{\tau_1}\right) + \frac{1}{6} \exp\left(-\frac{3t}{\tau_1}\right) + \frac{1}{3}. \quad (\text{A.14})$$

Due to the symmetrical nature of both the mixture operation and loading it is known that in an ideal system:

$$\begin{aligned} \hat{v}_{1,\text{blue}}(t) &= \hat{v}_{3,\text{red}}(t), \\ \hat{v}_{2,\text{blue}}(t) &= \hat{v}_{2,\text{red}}(t), \\ \hat{v}_{3,\text{blue}}(t) &= \hat{v}_{1,\text{red}}(t). \end{aligned}$$

Furthermore, from the definition of volume fraction we have:

$$\hat{v}_{i,\text{green}}(t) = 1 - \hat{v}_{i,\text{red}}(t) - \hat{v}_{i,\text{blue}}(t)$$

for each compartment i . Again acknowledging the mixer symmetry, it follows that:

$$\hat{v}_{1,\text{green}}(t) = \hat{v}_{3,\text{green}}(t) = \hat{v}_{2,\text{red}}(t) = \hat{v}_{2,\text{blue}}(t), \quad (\text{A.15})$$

$$\hat{v}_{2,\text{green}}(t) = \frac{2}{3} \exp\left(-\frac{3t}{\tau_1}\right) + \frac{1}{3} \quad (\text{A.16})$$